

Binary Interaction Can Yield a Diversity of Circumstellar Media around Type II Supernova Progenitors

TOMOKI MATSUOKA ^{1,2} AND RYO SAWADA ²

¹*Institute of Astronomy and Astrophysics, Academia Sinica, No.1, Sec. 4, Roosevelt Road, Taipei 10617, Taiwan, R.O.C.*

²*Department of Earth Science and Astronomy, Graduate School of Arts and Sciences, The University of Tokyo, Tokyo 153-8902, Japan*

(Received July 2, 2023; Accepted December 22, 2023)

Submitted to ApJ

ABSTRACT

Recent observations of supernovae (SNe) have indicated that a fraction of massive stars possess dense circumstellar medium (CSM) at the moment of their core collapses. They suggest the presence of additional activities of the SN progenitor driving the enhancement of the mass-loss rate, and some physical processes attributing to single star's activities have been considered. In this study, we carry out binary evolutionary simulations of massive stars by MESA and investigate effects on the subsequent CSM formation through hydrodynamical simulations by PLUTO. We show that the mass-transfer rate in a binary can increase at the beginning of the Roche lobe overflow, and this enhancement would be associated with the structure of the CSM before the explosion. We also illustrate that depending on the orbital period of the binary, the density structure of the CSM can have a diverse distribution including shell-like and cliff-like structures. These characteristic structures appear within the lengthscale of $\sim 10^{17}$ cm and could be traced by long-term observations of SNe, if the slow velocity of the CSM is assumed (~ 10 km s⁻¹). Our results highlight the importance of binary interaction in the aspect of reproducing the diversity of the CSM configuration.

1. INTRODUCTION

Mass loss from massive stars is one of the important elements in their stellar evolution so that it has a significant influence on the evolutionary characteristics and the fates of themselves (e.g., Yoon 2015). Understanding the physical properties of mass loss from massive stars would be a clue toward completing the construction of stellar evolution theory. Particularly, mass-loss activities prior to core-collapse supernovae (SNe) would be imprinted in the physical property of the circumstellar medium (CSM). This can contribute to the radiative source in SNe (see e.g., Kiewe et al. 2012; Smith 2017; Chevalier & Fransson 2017), and thus understanding the configuration of the CSM can also promote the precise modeling of SNe.

Thanks to the recent development of transient surveys and rapid follow-up observation systems, it has been recognized that there is a diversity of the CSM configura-

tion inferred for SN progenitors. For instance, it is implicated through optical flash spectroscopy experiments that a Type II SN progenitor is encompassed by a dense CSM confined within small lengthscale ($\sim 10^{15}$ cm. See e.g., SN 2013fs, SN 2023ixf, Yaron et al. 2017; Jacobson-Galan et al. 2023; Zimmerman et al. 2023). This is also supported by theoretical modelings of the early-phase optical light curve (Förster et al. 2018; Morozova et al. 2017; Moriya et al. 2017), as well as the detection of precursor activities before the SN (e.g., SN 2020tlf, Jacobson-Galán et al. 2022). Another example is that a few SNe are considered to undergo CSM interaction in the late phase (\sim several years after the explosion. See e.g., Weil et al. 2020; Kilpatrick et al. 2021, 2022). As an extreme example of the late-phase CSM interaction, it is argued that there are several objects exhibiting the transformation of the SN type from a stripped-envelope SN to a Type IIn SN (Margutti et al. 2017; Tinyanont et al. 2019; Tartaglia et al. 2021; Chandra et al. 2020), or showing the rebrightening of radio emission (Mauerhan et al. 2018; Balasubramanian et al. 2021; Maeda et al. 2023). These objects are speculated to have shell-

structured CSM detached from the progenitor, highlighting the possible mass ejection of the progenitor in the past (see the discussion in [Maeda et al. 2023](#)).

The CSM structure deviating from the steady wind configuration is thought to attribute to an enhanced mass-loss activity before the explosion. Since canonical stellar evolution theories do not expect a significant increase in the mass-loss rate before the SN explosion ([Langer 2012](#)), several mechanisms attempting the explanation of the increase in the mass-loss rate have been proposed, including the excitation of gravity wave in the convective core (e.g., [Quataert & Shiode 2012](#); [Shiode & Quataert 2014](#); [Smith & Arnett 2014](#); [Fuller 2017](#); [Morozova et al. 2020](#); [Wu & Fuller 2021](#); [Ko et al. 2022](#)). It should be noted that these attempts have focused on the properties of the stellar evolutionary behavior as a single star.

In this study, we simulate the stellar evolution in a binary system to calculate the pre-SN mass-loss rate of massive stars and propose the scenario that binary interaction can enhance the mass-loss rate from the binary system before the explosion. It is widely known that most massive stars are involved in a binary system that is about to undergo binary interaction ([Sana et al. 2012](#)). As the star evolves with time it experiences the expansion or contraction of the stellar radius at the moment of switching of the nuclear burning phases. If the star is involved in a tight binary so that the mass transfer between the stars can initiate, the mass exchange or the escape from the binary can affect the subsequent evolution of the primary star. In addition, the gas expelled from the binary system can be distributed around the SN progenitor as a CSM. Simulations of stellar evolution in binary systems have been examined in previous studies (e.g., [Ouchi & Maeda 2017](#); [Laplace et al. 2020, 2021](#)), but none of them have discussed CSM formation based on the mass-loss histories obtained therein. Through the demonstrations in this paper, we illustrate the variety of the CSM molded by binary interaction and suggest the possibility that this variety can give rise to the observational features of subsequent SNe seen a few years after the explosions. Our results shed light on the necessity to take into consideration the contribution of binary interaction to the formation of the CSM.

After the submission of this paper, we found that [Ercolino et al. \(2023\)](#) conducted a series of stellar evolutionary simulations to systematically survey the properties of long-period binaries of massive stars, which may largely overlap with the content of this paper. However, one of the pioneering points of this study is that we, for the first time, associate the activity of binary interaction with the formation of the CSM, which is en-

thusiastically investigated with the tool of hydrodynamical simulations. Another is that we attempt to give interpretations on time-variable mass-loss activities of SN progenitors in the framework of binary interaction.

This paper is organized as follows. In Section 2 the setup and procedure of our simulations are described. In Section 3 we show that for binary systems with specific parameter sets, a significant increase in the mass-loss rate before the SN explosion can be expected. We also demonstrate that the synthesized mass-loss history model can reproduce the inhomogeneous CSM structure deviating from the steady wind. In Section 4 we discuss possible physical processes that can alter our results. Especially, the dependence of the primary star’s initial mass is quantitatively investigated. Finally, we summarize the content of this paper in Section 5.

2. MODELS AND METHOD

Our study can be divided into two main parts: the estimation of the mass loss rate by binary evolution calculations using MESA, and the reconstruction of the CSM from this mass-loss history by hydrodynamic calculations using PLUTO. We show the setup of MESA for the binary evolution calculation in Section 2.1, and the results of the mass-loss rate estimation in Section 3.1. Similarly, the setup of the hydrodynamic calculations in PLUTO is shown in Section 2.2, and the results of the reconstruction of the CSM structure are in Section 3.2.

2.1. Setup of Stellar Evolution code MESA

We use stellar evolution code MESA in revision 15140 ([Paxton et al. 2011, 2013, 2015, 2018, 2019](#)) to solve stellar evolutions of both two stars in the binary from the zero-age main sequence (ZAMS). The computational setup and input parameters in MESA are mainly based on [Ouchi & Maeda \(2017\)](#), with some references to [Yoon et al. \(2010, 2017\)](#) and [Laplace et al. \(2020, 2021\)](#). Hereafter, we describe below the notable parts of this study.

We start the stellar evolutionary simulations with a non-rotating star for all the models. The initial ZAMS mass of the primary star is set to $M_1 = 12M_\odot$, which is a typical mass of the progenitor of a Type II supernova (e.g., [Smartt 2009](#)). The secondary star mass is fixed to $M_2 = 10.8M_\odot$, corresponding to the initial mass ratio of 0.9. We treat this mass ratio because, as pointed out in [Hurley et al. \(2002\)](#), small mass ratios ($q < 0.5$) cause unstable mass transfer, which makes computations difficult¹ (see also [Ouchi & Maeda](#)

¹ It should be noted that the mass ratio of Galactic O stars follows the uniform distribution, including binary systems with $q < 0.5$ (e.g., [Sana et al. 2012](#)).

2017). The initial orbital period is parametrized among $P_{\text{orb}} = 1100, 1300, 1500, 1700$ days. We adopt these values as the period for reproducing the progenitor of a Type II supernova affected by the binary interaction (Ouchi & Maeda 2017). We stop our simulation at the moment of the central carbon depletion $t_{\text{end}} = t_{\text{C,dep}}$. Here the central carbon depletion is defined as the moment when the mass fraction of carbon in the core falls below 10^{-6} (see also Section 2.1.3 and Appendix A). This definition is enough for our purpose because it takes only ~ 10 years from the moment of the central carbon depletion to the core collapse t_{cc} (see Appendix A and Figure A1 for the detail), which is shorter than stellar behaviors under consideration.

In order to construct robust stellar models in terms of spatial resolution, we fix a MESA parameter `max_dq` = 5×10^{-4} . This choice allows us to resolve the mass shell in the star at least $\sim 0.006 M_{\odot}$, satisfying the requirement of Farmer et al. (2016) that the mass resolution of $\sim 0.01 M_{\odot}$ is desirable for the convergence of the evolution of the star during the main-sequence phase. Hereafter we describe the detailed setups for physical processes directly relevant to our stellar evolutionary simulations. We also refer readers interested in the detailed settings to our inlists uploaded in Zenodo².

2.1.1. Metallicity and opacities

All the models are assumed at solar metallicity ($Z = 0.02$, where Z is the mass fraction of elements heavier than helium; Asplund et al. 2009). We employ the opacity tables from OPAL (Iglesias & Rogers 1996).

2.1.2. Atmosphere

The radius of a star is defined as the location satisfying $\tau = 2/3$. In MESA, the hydrostatic equilibrium equation is integrated with the Eddington grey $T - \tau$ relation, on the assumption of the plane-parallel limit (Eddington 1926). This allows us to obtain the surface boundary condition.

2.1.3. Nuclear reaction network

We employ the nuclear reaction network provided by MESA under the name `co_burn.net`, which includes ^1H , ^3He , ^4He , ^{12}C , ^{14}N , ^{16}O , ^{20}Ne , ^{24}Mg , and ^{28}Si . This is applicable for stellar evolutions up to the oxygen-burning phase (Timmer 1999). We adopt the nuclear reaction rates in the default version of the MESA, taken from NACRE (Angulo et al. 1999) and JINA REACLIB (Cyburt et al. 2010).

² <https://doi.org/10.5281/zenodo.8385153>

We note that after the central carbon depletion, the dynamical timescale of the star can be shorter than the lifetime left, and even the behavior of the primary star as a single star remains a matter of debate (e.g., Woosley et al. 2002; Arnett & Meakin 2011). For this reason, we use a simple and computationally inexpensive network sufficient to calculate stellar evolution until the carbon-burning phase.

2.1.4. Mixing

For the treatment of convective mixing, we use the mixing length theory (MLT) approximation (Henyey et al. 1965) with a mixing-length parameter of $\alpha_{\text{MLT}} = 2.0$. The Ledoux criterion for convection is used, and semi-convection following Langer et al. (1985) is employed with an efficiency parameter $\alpha_{\text{sc}} = 1.0$ (Yoon et al. 2010). We apply the overshooting for the convective core and shell experiencing hydrogen burning, and also for the convective core and shell where no significant burning takes place. The overshoot is realized by exponentially decaying the convective diffusion coefficient from the convective boundary according to Herwig (2000) (see also Paxton et al. 2013 for detail). We take an overshooting parameter as $0.016H_p$, where H_p is the pressure scale height evaluated at the radius near the boundary of the convective core (with $f = 0.018$ and $f_0 = 0.002$). Although MESA has options to include other kinds of mixing processes (e.g., thermohaline mixing, rotational mixing, and extra mixing), these are not considered in this study.

2.1.5. Wind

For the stellar wind, we follow the ‘Dutch’ wind scheme implemented in MESA with a scaling factor fixed to 1.0. The ‘Dutch’ wind scheme in MESA combines the results from several papers. For cool stars with effective temperatures $T_{\text{eff}} < 10^4$ K, we apply the wind scheme in de Jager et al. (1988).³ This prescription is validated through observations of galactic red supergiants (Mauron & Josselin 2011). For hot stars with the effective temperature $T_{\text{eff}} > 10^4$ K, we adopt two formulae depending on the surface mass fraction of hydrogen $X_{\text{H,surf}}$; we use the formula suggested in Vink et al. (2001) for hydrogen-rich stars ($X_{\text{H,surf}} > 0.4$), while we use the recipe of Nugis & Lamers (2000) for hydrogen-poor stars ($X_{\text{H,surf}} < 0.4$).

2.1.6. Binary System

³ We note that there is still a debate on the uncertainty of the mass-loss rate of cool stars. See e.g., Beasor et al. (2020) for the recent analysis.

In binary systems, we consider only non-conservative mass transfer. Our calculations include the loss of angular momentum due to the binary motion, such as mass loss. We assume that all of the angular momentum loss in the binary system occurs from the vicinity of the accretor star (see [Soberman et al. 1997](#); [Paxton et al. 2015](#)). This causes the period of the binary system to evolve in time from the initial period, but these detailed dependencies are beyond the scope of this paper. The Roche lobe radius of the primary star is calculated following the [Eggleton \(1983\)](#) method,

$$R_{\text{RL},1} = \frac{0.49q^{2/3}}{0.6q^{2/3} + \ln(1 + q^{1/3})} a, \quad (1)$$

where $q = M_1/M_2$ is the mass ratio and a is the binary separation expressed as

$$a = \left(\frac{G(M_1 + M_2)P_{\text{orb}}^2}{4\pi^2} \right)^{1/3}, \quad (2)$$

where G is the gravitational constant. When one of the stars in the binary system initiates Roche lobe overflow, we implicitly compute the mass-transfer rate using the prescription described in [Kolb & Ritter \(1990\)](#). Here, we introduce the accretion efficiency parameter β ([Tauris & van den Heuvel 2006](#)), which prescribes the fraction of the gas accreting onto the secondary star relative to the gas lost from the primary star due to the binary stripping. In other words, we have the following relationship between the total mass-loss rate of the primary star \dot{M}_1 , the mass-transfer rate between the binary system \dot{M}_{tr} , and the mass outflow rate into the CSM \dot{M}_{CSM} ;

$$\dot{M}_1 = \dot{M}_{\text{wind},1} + \dot{M}_{\text{tr}}, \quad (3)$$

$$\dot{M}_{\text{CSM}} = \dot{M}_{\text{wind},1} + (1 - \beta)\dot{M}_{\text{tr}}, \quad (4)$$

where $\dot{M}_{\text{wind},1}$ is the mass-loss rate due to the stellar wind of the primary star. We neglect the contribution of the stellar wind from the secondary star. This is because it remains in the main sequence during the simulations so that the mass and momentum budgets belonging to the stellar wind from the secondary star are smaller than those from the primary star itself and the gas under the transfer.

2.2. Hydrodynamics of the CSM formation

We adopt the code PLUTO ([Mignone et al. 2007, 2012](#)) to solve the equations of hydrodynamics in one-dimensional spherical coordinates. We prepare the simulation domain from the inner boundary radius $r_{\text{in}} = V_w(t_{\text{cc}} - t_{\text{end}}) \simeq 3 \times 10^{13}$ cm ($V_w/10$ km s $^{-1}$) to $r_{\text{out}} = 10$ pc ($\simeq 3 \times 10^{19}$ cm) and divide the domain into 256

meshes in the logarithmic scale where V_w is the value of the velocity of the gas flowing from the binary system. Here we assume $t_{\text{cc}} - t_{\text{end}} = 10$ years (see also Section 2.1). As an initial profile we consider the thermodynamic quantities $\rho = 1.6 \times 10^{-24}$ g cm $^{-3}$ (corresponding to the number density of $n = 1$ cm $^{-3}$), $T = 10^4$ K to mimic warm interstellar medium ([Draine 2010](#)). The outflow condition is applied to the outer boundary in the simulation domain.

By injecting the gas from the inner boundary following the model for the mass-loss history obtained in Section 2.1, we can construct the hydrodynamical structure of the CSM. We need to assume the value of V_w ; there is uncertainty as to what the realistic values of the velocity of the gas escaping from the binary system should be. The reasonable choice would be the velocity comparable to the escape velocity of the central object ($V_w \sim V_{\text{esc}} \propto R_*^{-1/2}$, where R_* is the stellar radius). $V_w \sim \mathcal{O}(10)$ km s $^{-1}$ would be expected if the escape velocity of the inflated primary star gives a main contribution, while $V_w \sim 1000$ km s $^{-1}$ might be possible in a case where the gas is coming from the compact secondary star. We examine the value of $V_w = 10, 100,$ and 1000 km s $^{-1}$ and apply these parameters for the simulation of the CSM formation in the binary models in Section 2.1. The CSM density at the inner boundary radius r_{in} is given as

$$\rho_{\text{inj}} = \frac{\dot{M}_1}{4\pi r_{\text{in}}^2 V_w}. \quad (5)$$

The structure within the inner boundary would be determined by the progenitor activity after $t \sim t_{\text{end}}$, which we do not investigate in detail.

It is also possible to examine the CSM formation by making use of the analytic treatment on the time-dependent wind dynamics as presented in [Piro & Lu \(2020\)](#). This is applicable as long as the ram pressure of the wind surpasses the thermal pressure of the ambient medium swept by the wind. Once these two pressures become comparable to each other, the ambient medium will suppress the expansion of the wind and the shocked wind gas begins to accumulate at the contact discontinuity between the wind and the medium, deviating from the analytical solution ([Weaver et al. 1977](#); [Matsuoka et al. 2022](#)). To investigate large-scale structure of the CSM in the framework of binary interaction, we rely on numerical hydrodynamical simulations in this study. A similar method is employed in the context of numerical simulations of supernova remnants ([Tenorio-Tagle et al. 1990, 1991](#); [Dwarkadas 2005, 2007](#); [Yasuda et al. 2021, 2022](#); [Matsuoka et al. 2022](#)). In addition, the choice of the large outer radius of the simulation domain

$r_{\text{out}} = 10 \text{ pc}$ allows us to find out the difference between numerical and analytical treatments, which is discussed in Appendix B.

3. RESULT

In this section, we describe the results of our stellar evolutionary simulation and the expected CSM configuration. For convenience, we define the look-back time $t_{\text{lb}} = t_{\text{cc}} - t$ as an indicator of the evolutionary phase of the star.

3.1. Binary evolution

Table 1 shows the summary of the total stellar mass and the hydrogen envelope mass of the primary star, and the CSM mass in our binary models at the end of the simulations. We can observe a tendency for the total mass of the star and the hydrogen envelope to become smaller as the orbital period is shortened, because a tighter binary suffers more strong binary interaction. We can estimate the ejecta mass of the subsequent SNe at several solar masses for all of the models by subtracting the mass of a newborn neutron star from the final stellar mass. This could be smaller than the median value of Type II-P SNe containing a large amount of the hydrogen envelope (Martinez et al. 2022), but typical for the SNe II got rid of some fractions of the hydrogen envelope, such as Type II-L and II-b SNe (Bersten et al. 2012; Moriya et al. 2016).

Figure 1 shows the time evolution of the mass loss rate (\dot{M}_1) and Roche lobe radius ($R_{\text{RL},1}$) of the primary star in the binary models with the orbital period $P_{\text{orb}} = 1100, 1300, 1500, 1700$ days. The time evolution of the mass-loss rate can be interpreted in the basic framework of the binary evolution (e.g., Ouchi & Maeda 2017). We can see that the models with $P_{\text{orb}} = 1100, 1300, 1500$ days experience a drastic increase in the mass-loss rate. The timings of the increase in \dot{M}_1 coincide with the moment when the primary star fills the Roche lobe radius. Our simulations suggest that even without introducing the single star's activity arising eruptions (e.g., Shiode & Quataert 2014; Fuller 2017; Wu & Fuller 2021; Ko et al. 2022), an SN progenitor involved in a binary can boost the mass-loss rate from the system at the moment of the expansion of the stellar radius.

Firstly, we start the detailed discussion in the model with $P_{\text{orb}} = 1300$ days as an example. The left panel in Figure 1 shows the time evolution of characteristic mass-loss rates and the radii in the primary star. They show that the primary star experiences a mass loss by the stellar wind in the hydrogen-burning phase ($t_{\text{lb}} \gtrsim 10^6$ years). Then, due to the increase in the stellar luminosity in addition to the decrease in the effective

temperature after the core hydrogen burning, the stellar wind mass loss rate increases by 30 times around $t_{\text{lb}} \sim 10^6$ years, while the Roche lobe overflow does not occur at the time in this model. At $t_{\text{lb}} \sim 2 \times 10^4$ years the helium burning in the stellar core ends, and the primary star expands again (see the bottom right panel in Figure 1). At this timing, the stellar radius reaches the Roche lobe radius and the binary mass transfer begins. The mass transfer rate then rapidly increases up to $10^{-2} M_{\odot} \text{ yr}^{-1}$, and the mass of the primary star reduces down to $M_1 \sim 6 M_{\odot}$. The second bump in the mass transfer history can be seen at $t_{\text{lb}} \sim 5000$ years. This could be associated with the single stellar activity of the primary star, since the evolution of the single star with the same initial mass (black dashed line in the left bottom panel of Figure 1) also shows the slight expansion of the stellar radius at $t_{\text{lb}} \sim 5000$ years (see also Section 4). After that, the Roche lobe overflow continues until the core collapse, while the mass-transfer rate is regulated down to $\sim 10^{-5} M_{\odot} \text{ yr}^{-1}$.

We note that the primary star in the binary model is inflating more than the single star. This is caused by the mass reduction through the Roche lobe overflow after the full growth of the stellar core. We can understand the behavior of the stellar radius on the basis of the energy balance between the gravitational energy and the internal energy of the star, as explained by the Virial theorem (Kippenhahn & Weigert 1990, or see Appendix C for the quantitative interpretation). The internal energy of the star is mainly determined by the thermodynamical state of the stellar core (Laplace et al. 2021). During the Roche lobe overflow in our binary models, the primary star settles in the helium-burning stage, implying sufficient growth of the stellar core. Thus, both the primary star in the binary model and the single star should have similar internal energies at $t_{\text{lb}} \lesssim 10^5$ years. In contrast, the reduction of the stellar mass through mass transfer in the binary results in an increase in the gravitational energy of the star. Consequently, the primary star in the binary can easily expand the radius larger than the star without the companion star.

Comparing the evolutions of a single star with the star in a binary can be a clue to understanding the critical physical processes in a binary system. The radius of the primary star in the binary follows the same path as that evolving as a single star until it first fills the Roche lobe radius. This implies that the timing when a star first fills the Roche lobe radius can be roughly understood through the comparison between the Roche lobe radius and the radial evolution in the single stellar evolution (see later).

Table 1. Summary of physical quantities in this system, especially for the terminal state of the primary star.

initial period P_{orb} [days]	final mass $M_{1,f}$ [M_{\odot}]	H-envelope mass $M_{\text{env},f}$ [M_{\odot}]	CSM mass for $V_w = 10\text{km s}^{-1}$ M_{CSM} [M_{\odot}]	CSM mass for $V_w = 1000\text{km s}^{-1}$ M_{CSM} [M_{\odot}]
1100	4.8	1.3	1.4	0.3
1300	5.9	2.4	5.0	0.6
1500	7.2	3.7	3.8	0.9
1700	10.8	7.3	0.05	0.02
single star	10.8	7.3	0.05	0.02

NOTE— The ‘final mass’ refers to the total stellar mass of the primary star and ‘H-envelope mass’ is defined as the amount of the hydrogen envelope in the primary star. The CSM mass is defined as the enclosed mass within the radius at which the CSM distribution reconstructed through the analytical treatment matches well with that through the numerical simulation (see Appendix B). All of the mass budgets are computed with quantities at the end of the simulation (i.e., at the moment of the central carbon depletion of the primary star).

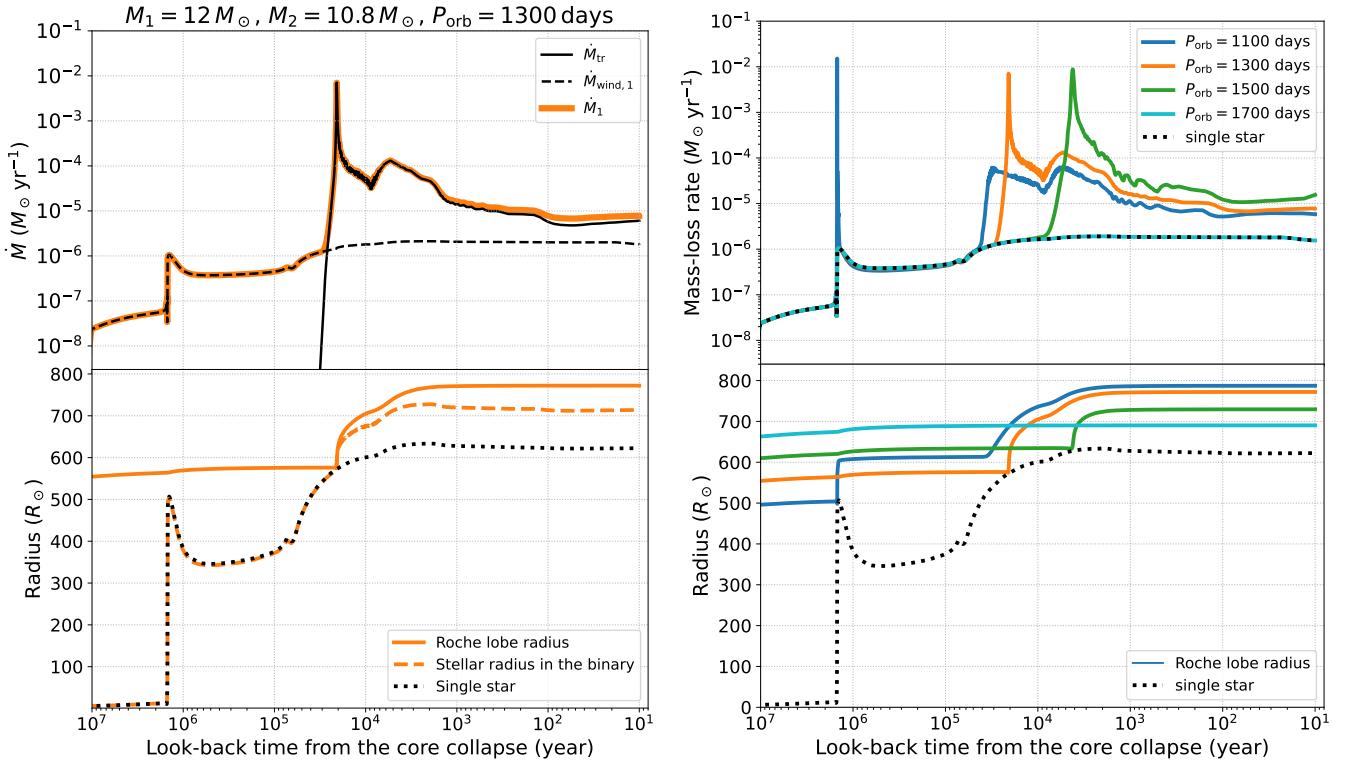


Figure 1. Left: Time evolution of the mass-loss history (top) and the characteristic radii (bottom) as a function of the look-back time for the binary models with $P_{\text{orb}} = 1300$ days. In the top panel the mass-loss rate is decomposed into the components of the stellar wind and the mass transfer to the secondary star in the top panel. In the bottom panel, the time evolutions of the Roche lobe radius and the stellar radius of the primary star are illustrated, in addition to the $12 M_{\odot}$ single star’s radius. Right: The total mass-loss rate histories and the Roche lobe radii for the binary models with $P_{\text{orb}} = 1100, 1300, 1500, 1700$ days are shown.

The right panel of Figure 1 shows the dependence of mass loss properties on the orbital period P_{orb} . In all binary models, the primary star will eventually become a Type II SN progenitor because the primary star retains the hydrogen envelope until the core collapse (see Table 1). We can see the trend that the longer the initial orbital period P_{orb} , the further the timing of the Roche

lobe overflow is delayed. When the initial orbital period is too long ($P_{\text{orb}} > 1700$ days), the mass loss rate is roughly the same as the mass loss rate in single stellar evolution, since the binary does not experience Roche lobe overflow (see dashed black line and solid cyan line in the right panel of Figure 1).

It is possible to compare the binary models with $P_{\text{orb}} = 1100, 1300,$ and 1500 days to the single stellar evolution. All binary models follow the same evolutionary path as the single stellar model until $t_{\text{lb}} \sim 10^6$ years. The model of $P_{\text{orb}} = 1500$ days follows almost similar evolution to the model of $P_{\text{orb}} = 1300$ days discussed above, except that the Roche lobe overflow starts slightly later due to the larger Roche lobe radius. The model with $P_{\text{orb}} = 1100$ days undergoes a Roche lobe overflow after the end of the core hydrogen burning at $t_{\text{lb}} \sim 10^6$ years, which leads to the release of about $\sim 7 M_{\odot}$ of the hydrogen outer layer. It then experiences another Roche lobe overflow at $t_{\text{lb}} \sim 3 \times 10^4$ years, following a path different from that in single stellar evolution. However, we should emphasize that it is no coincidence that $P_{\text{orb}} = 1100$ days model exhibits the mass-loss enhancement at $t_{\text{lb}} \sim 10^4$ years similarly to the other binary models ($P_{\text{orb}} = 1300, 1500$ days). Normally, helium burning in the stellar core ends at $\sim 10^4$ years before the core collapses (e.g., Woosley et al. 2002). At this time, the primary star expands again, and thus we can see an enhancement of mass loss.

We note the model of $P_{\text{orb}} = 1700$ days follows the same mass loss history as the single stellar model since the primary star radius remains sufficiently smaller than its Roche lobe radius in the whole of the lifetime of the star. Therefore, while we conducted the CSM reconstruction even for the binary model with $P_{\text{orb}} = 1700$ days, we do not discuss the result of the model in the next section.

3.2. Reconstruction of CSM

Figure 2 shows the density structures of the CSM for the binary models assuming $V_w = 10 \text{ km s}^{-1}$. We can see that the shell-like distribution is standing out at $\sim \mathcal{O}(10^{17})$ cm in the models with $P_{\text{orb}} = 1300, 1500$ days. The corresponding look-back time is around $t_{\text{lb}} \sim 10^4$ years and it is easily found that at that time the mass-loss rate is enhanced by orders of magnitude, compared to that expected for the steady wind of a red supergiant (RSG). As for the model with $P_{\text{orb}} = 1100$ days, not shell-like but the cliff-like structures in the CSM are appearing at the radii of 2×10^{17} cm and 10^{18} cm. These features are associated with the mass-loss enhancements at $t_{\text{lb}} \sim 5000$ years and 3×10^4 years, respectively. We suggest that binary interaction can give rise to the formation of the shell-like and cliff-like CSM structures.

We confirm that there is no mixing of heavy elements into the hydrogen envelope of the primary stars within the parameter range of this study. Also as can be seen from Table 1, the mass release from the primary star happens only from the hydrogen layer, not from the he-

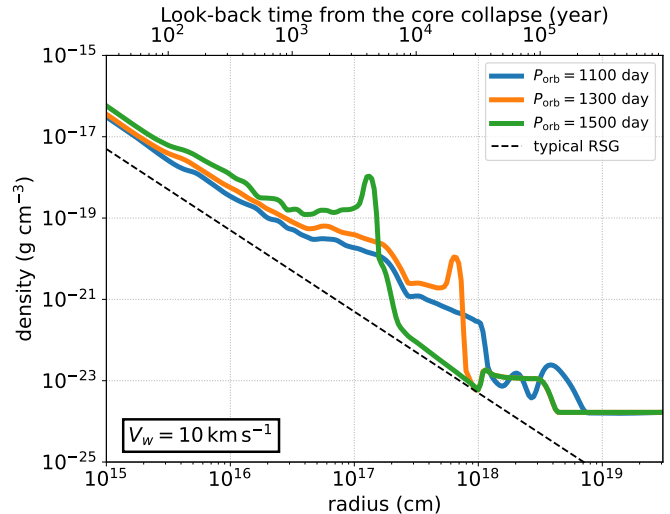


Figure 2. Density structures of the CSM in the binary models with $P_{\text{orb}} = 1100, 1300, 1500$ days reconstructed on the assumption of the wind velocity $V_w = 10 \text{ km s}^{-1}$. The dashed line stands for the typical steady wind distribution expected for a red supergiant ($\dot{M} = 10^{-6} M_{\odot} \text{ yr}^{-1}$, $V_w = 10 \text{ km s}^{-1}$).

lium core. Therefore, the CSM composition is expected to be similar to that of Sun.

The dependence of the CSM structure on the wind velocity is also worth investigating, which is shown in Figure 3. We can see that higher wind velocity leads to the widely distributed and thin-density structure of the CSM. As V_w becomes faster, the wind can reach the lengthscale farther from the SN progenitor, while its density becomes smaller (see equation 5). We note that the shell-like component in the model with slower wind velocity lies in the smaller lengthscale.

The variety of hydrodynamical structures of CSM would give rise to observational characteristics of subsequent SNe, such as the excess in the optical emission and the re-brightening of radio emission in the late phase of SN-CSM interaction (e.g., Weil et al. 2020; Kilpatrick et al. 2022; Maeda et al. 2023). Here we discuss the possibility that our results can give explanations for characteristics of SNe indicated by late-phase observations. If the wind velocity is as slow as orders of $\sim 10 \text{ km s}^{-1}$, then the location of the mass shell observed in the model with $P_{\text{orb}} = 1300, 1500$ days falls in $\sim 10^{17}$ cm. This could be an origin for the observational signature of late-time SN-CSM interaction seen in several Type II SNe because the SN shock begins interacting with the shell at the radius of $\sim 10^{17}$ cm a few years after the explosion. To quantitatively discuss the variation of the CSM density in the radial direction, mass-loss rate of SN progenitor can serve as an indicator of the density variation

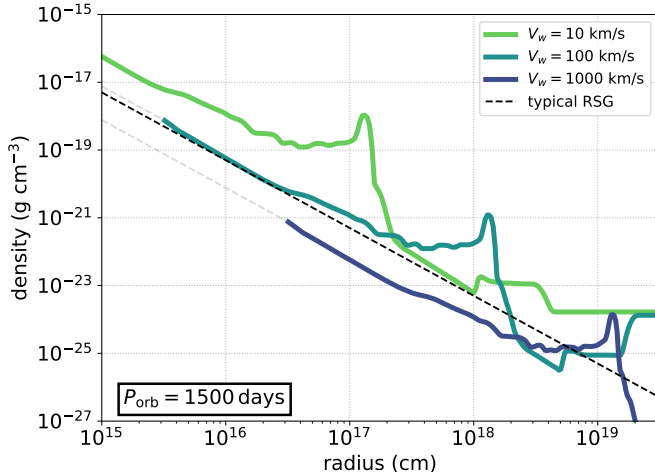


Figure 3. Density structures of the CSM in the binary models of $P_{\text{orb}} = 1500$ days with the velocity varied among 10, 100, and 1000 km s^{-1} . The dashed line within $r < 3 \times 10^{15}$ cm in the model of $V_w = 100 \text{ km s}^{-1}$ and $r < 3 \times 10^{16}$ cm in the model of $V_w = 1000 \text{ km s}^{-1}$ denote the components of the CSM with their corresponding look-back timescale less than t_{cc} , during which we do not explore. The black dashed line shows a steady wind structure expected for a red supergiant, the same as the one in Figure 2.

of the CSM. Maeda et al. (2021) argues that the variation in the mass-loss rate only by a factor can emerge as an observational peculiarity in radio light curves of SNe. Maeda et al. (2023) also suggests that the elevation of the mass-loss rate by an order of magnitude could be an explanation for the radio re-brightening of SNe. Other cases are that Weil et al. (2020) and Kilpatrick et al. (2022) ascribe the origin of the excess in the optical light curves as the existence of the CSM with their mass-loss rates not so much higher ($\dot{M} \sim 10^{-7} - 10^{-6} M_{\odot} \text{ yr}^{-1}$), but these densities are enough for the appearance of the observable CSM interaction features. As for our binary models reproducing shell-like CSM structures, their density variations range from factors to an order of magnitude, and we expect these variations enough to be ascribed as the origin for the CSM interaction features observed in late-phase SNe.

The cliff-like structure seen in the model of $P_{\text{orb}} = 1100$ days can be also intriguing since the cliff-like structure may lead to the attenuation of the CSM interaction signature in the late phase of SNe. Indeed, Weiler et al. (2007) reported a steep dimming in the radio emission from SN 1993J ~ 10 years after the explosion. They further suggested that the mass-loss rate increased up to at least 3 times ~ 8000 years before the explosion, corresponding to the lengthscale of the CSM of 2×10^{17} cm. Our model with $P_{\text{orb}} = 1100$ days exhibits a density variation comparable to or even higher than the above

implications, supporting that our binary models can be likely to give rise to CSM interaction features sufficiently prominent to be traced by observations. We also note that the binary interaction scenario is consistent with the fact that SN 1993J is a Type IIb SN originating from a massive star probably suffered from the stripping of the envelope by a companion star (e.g., Maund et al. 2004).

In addition to implications from SN observations, we also note that direct observations of late-type stars in our galaxy indicated the existence of the multiple-shell structure in the circumstellar environment due to the binarity (Mauron 1997; Mauron & Huggins 1999). This supports that binary interaction can be a feasible origin of the emergence of the shell-like structure in the circumstellar environment of stars Mauron (1997); Mauron & Huggins (1999).

4. DISCUSSION

In the previous section, we have mainly discussed the relationship between stellar evolution in a binary and the CSM formation. Yet, there are some physical processes and parameter spaces that have not been explored or considered in detail. In this section, we discuss the mass dependence of the primary star (Section 4.1), the binary evolution with the short orbital period reproducing stripped-envelope SNe (Section 4.2), and some caveats relevant to CSM formation associated with binary interaction (Section 4.3).

4.1. Diversity of the binary evolution and its dependence on the mass of the primary star

In this study, we fixed the value of the initial primary mass to clarify the physics of the CSM formation. Our results show that the CSM properties depend on the evolution of the primary star radius R_1 , as well as several physical parameters such as P_{orb} and V_w . Obviously, the radial evolution of the primary star depends on the choice of the initial primary mass, and the variation of the primary mass expands the diversity of stellar evolution itself. Here, we present a series of models in which the initial primary mass is parametrized, and discuss the effect of the variation of the primary mass on the behavior of the mass-loss history and the resultant CSM structure qualitatively.

Here we note the purpose of this section. We will show how different primary masses, i.e., different stellar evolutions of the primary stars, give rise to different mass loss activities and CSM structures. This is because the evolution of mass loss due to binary interaction strongly reflects the stellar evolution of the primary star peculiar to itself, as studied for the case of the primary star mass

of $M_1 = 12M_\odot$ in Section 3. Detailed analysis of the results in this section would necessitate individual stellar evolution calculations, which are beyond the scope of this paper. Hence, we just limit our discussion to showcasing an example of the diversity resulting from different primary star masses.

Figure 4 shows the time evolution of the mass loss rate (\dot{M}_1) adopted for the primary star masses $M_1 = 14.4, 15, 16.2M_\odot$. Other physical/binary parameters are fixed; the orbital period $P_{\text{orb}} = 1900$ days and the secondary mass $M_2 = 13.5M_\odot$. We have confirmed that in all of these models, the primary star will eventually become a Type II SN progenitor encompassed by a hydrogen envelope. We can see that the models with $M_1 = 15M_\odot$ experience the drastic increase in the mass-loss rate at $t_{\text{lb}} \sim \text{a few} \times 10^3$ years. Also, the models with $M_1 = 16.2M_\odot$ shows the multiple episodes in the mass-loss history around $t_{\text{lb}} \sim 3 \times 10^4, 10^4$ and 10^2 years. On the other hand, in the models with $M_1 = 14.4M_\odot$, no mass-loss gain is observed even though the same orbital period and secondary mass are employed.

We suppose that the differences among the three models are attributed to the behaviors of the primary star. In the evolutionary stage after the carbon burning, the stellar radius can be variable due to single stellar activity, such as shell flashes and core convection. When the star is evolving as a single star, these activities would not be reflected in the mass-loss history unless they induce mass loss from the surface of the star (e.g., Quataert & Shiode 2012; Shiode & Quataert 2014). This is true even when the primary star is in a binary but its Roche lobe radius is sufficiently larger than the stellar radius (the case of $M_1 = 14.4M_\odot$). However, when the Roche lobe radius becomes comparable to the stellar radius of the primary star, the radial variation of the star would be reflected in the mass loss due to Roche lobe overflow, and thus the complicated evolution of the mass-loss rate would be realized. In other words, binary interaction plays a role in enhancing the stellar behavior of the primary star as a form of mass-transfer history. We expect that the difference in the evolution of the stellar radius between $M_1 = 15M_\odot$ and $16.2M_\odot$ results in the difference in the mass-transfer history. We propose that single stellar activities that involve the expansion of the stellar radius but do not induce mass eruptions, may also contribute to mass loss if the star is in a binary system. Thus, understanding the massive star’s evolution after the carbon-burning phase would be important even for seeking the origin of the dense-CSM structure around SN progenitors.

The mass-loss histories drawn in Figure 4 are informative even for the formation of the resultant CSM

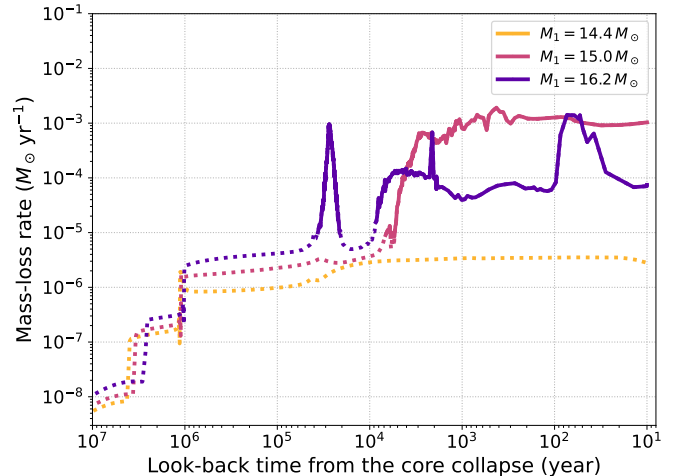


Figure 4. Time evolutions of mass-loss rates in binary systems with $M_1 = 14.4M_\odot, 15.0M_\odot$, and $16.2M_\odot$ are plotted by dotted lines. In addition, the epochs are highlighted by solid lines when the mass-transfer rate is greater than the mass-loss rate of the stellar wind. The secondary star’s mass and the orbital period are set to $M_2 = 13.5M_\odot$ and $P_{\text{orb}} = 1900$ days, respectively.

structure. As examples, we take up the models with $M_1 = 15.0M_\odot$ and $M_1 = 16.2M_\odot$. First, we propose that binary interaction can be one of the origins producing dense CSM inferred in Type IIIn SNe. We can see that the mass-loss rate seen in the model with $M_1 = 15.0M_\odot$ is elevated to $\sim 10^{-3}M_\odot \text{ yr}^{-1}$ from a few thousand years before the explosion. This is comparable to those previously inferred for Type IIIn SNe (e.g., Kiewe et al. 2012; Moriya et al. 2014), and in good agreement with the discussion in Ouchi & Maeda (2017). If we consider the slow velocity of the CSM ($V_w = 10 \text{ km s}^{-1}$), the CSM in this model is expected to have a cliff-like structure; a steep density drop at the radius of $\sim 10^{17} \text{ cm}$. This lengthscale may be consistent within a factor with the implication of Katsuda et al. (2016), where some Type IIIn SNe are suggested to be encompassed by a torus-like CSM truncated at around several times of 10^{16} cm .

Another suggestion is that binary interaction in the final evolutionary phase can be a possible explanation of the signature of the CSM interaction observed in infant SNe. Figure 5 shows the synthesized CSM structure for the model with $M_1 = 16.2M_\odot$. The mass-loss history of this model is characterized by multiple enhancements of the mass-loss rate. The last mass-loss episode happens at $t_{\text{lb}} \sim 50$ years, and the gas expelling from the binary system at that episode would reach out to $\sim 10^{15} \text{ cm}$. We remark that this lengthscale may be compatible with that inferred for the confined CSM seen in some infant Type II SNe (see e.g., Yaron et al. 2017 for SN 2013fs,

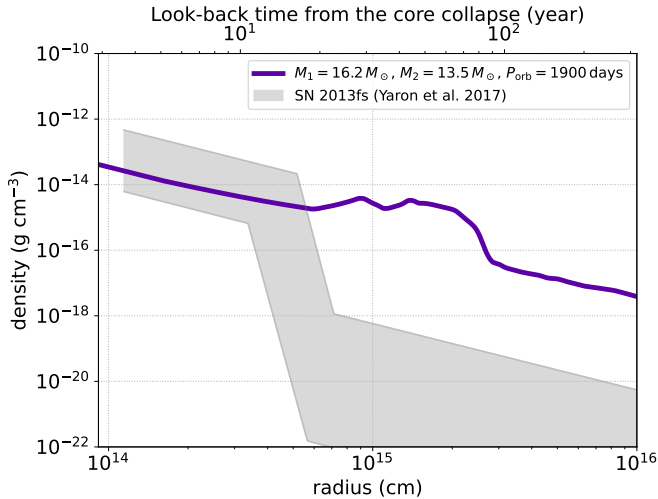


Figure 5. The synthesized CSM density structure for the model with $M_1 = 16.2 M_\odot$, $M_2 = 13.5 M_\odot$, and $P_{\text{orb}} = 1900$ days, assuming the wind velocity $V_w = 10 \text{ km s}^{-1}$. Gray shaded region illustrates the possible parameter space for the CSM properties inferred for SN 2013fs (Yaron et al. 2017).

Jacobson-Galán et al. 2022 for SN 2020tlf, and Zimmerman et al. 2023 for SN 2023ixf). We note a caveat that our model is not quantitatively tuned to the observational implication represented by SN 2013fs, and the discussion should be limited qualitatively. Nevertheless, we advocate that the binary interaction episode arising $\lesssim 100$ years before the explosion can leave an inhomogeneous structure in the vicinity of the SN progenitor and it may contribute to the unique observational features of infant Type II SNe such as flash spectroscopy and early excess of optical light curve (Yaron et al. 2017; Morozova et al. 2017; Moriya et al. 2017; Jacobson-Galán et al. 2022).

4.2. Reproducing mass-loss histories of stripped-envelope SN progenitors

A stripped-envelope SN is indicated to originate from a binary system (e.g., Lyman et al. 2016; Fang et al. 2019). There are also suggestions that some stripped-envelope SNe produce a sign of the interaction between the massive shell-like CSM in the late phase of the SNe (Margutti et al. 2017; Mauerhan et al. 2018; Balasubramanian et al. 2021), and this implication looks consistent with our results. In fact, some binary evolutionary simulations with short orbital periods of $P_{\text{orb}} \lesssim 10$ days through Case A or Case BB mass transfers have been successful in reproducing models for stripped-envelope SN progenitors (Ouchi & Maeda 2017; Gilkis et al. 2019; Laplace et al. 2020), although there has been less attention to mass-transfer histories.

We attempted binary evolutionary simulations of such a short-period system with the same stellar masses of the stars by using the mass-transfer prescription following Hurley et al. (2002). We found that the mass-transfer rate is intensely fluctuating by orders of magnitude within short timescales. This fluctuation has been observed in the previous works (see Figure 8 in Paxton et al. 2015) and it prevents us from understanding the features of the mass-transfer history in a tight binary, which we will postpone in future work. However, it may be notable that Wu & Fuller (2022) conducted the stellar evolutionary simulations of low-mass He stars accompanied by a neutron star, and the obtained mass-loss rates therein are not fluctuated.

4.3. Other physical processes affecting CSM formation

This study aims to construct CSM models originating from binary interaction, but there are several assumptions and other possible physical processes that could affect our result. This section discusses their roles in characterizing CSM properties and assesses their importance.

- **The timing of the termination of stellar evolutionary simulations**

We assume that the primary star experiences core collapse $t_{\text{end}} - t_{\text{cc}} = 10$ years after entering the central carbon depletion stage. Notice that our definition of the central carbon depletion stage is the phase when the mass fraction of carbon in the core falls below 10^{-6} . Based on this definition, we believe that the time span from the central carbon depletion stage to the core collapse would not be largely modified depending on stellar quantities by orders of magnitude. Actually, our definition of the central carbon depletion stage corresponds to the epoch just before the ignition of oxygen burning in the core (Tur et al. 2010). Even if there are variations in $t_{\text{end}} - t_{\text{cc}}$ by factors, it should affect the neighborhood circumstellar environment of SN progenitors with the lengthscale of $V_w(t_{\text{end}} - t_{\text{cc}}) \sim 3 \times 10^{14} \text{ cm}$ on the assumption of $V_w = 10 \text{ km s}^{-1}$. This is sufficiently shorter than the characteristic CSM lengthscales discussed in Section 3.2.

- **Thermodynamical state of external interstellar medium**

This study assumes warm interstellar medium ($\rho = 1.6 \times 10^{-24} \text{ g cm}^{-3}$, $T = 10^4 \text{ K}$) as an initial condition of simulations of CSM formation, whereas it is known that interstellar medium can take various phases including dense or dilute environment (Draine 2010). However, if we focus on

observational timescale of SNe and lengthscale of CSM ($t \lesssim$ a few years or $r \lesssim 10^{17}$ cm), it does not matter because the characteristics of CSM is predominantly determined by the bulk properties of the outflow from the Roche lobe overflow. If anything, the difference of the interstellar medium state affects the large-scale structure of the CSM that may influence the evolution of supernova remnants (Yasuda et al. 2021, 2022; Matsuoka et al. 2022). We also investigate CSM formation properties with the different initial conditions such as cold ($\rho = 1.6 \times 10^{-22}$ g cm $^{-3}$, $T = 10^2$ K) and hot ($\rho = 1.6 \times 10^{-26}$ g cm $^{-3}$, $T = 10^6$ K) interstellar medium. We confirm that the choice of the thermodynamical state of the interstellar medium does not have an influence on the resultant CSM configuration in the region of which we are interested ($r \lesssim 10^{18}$ cm). Basically, the existence of the interstellar medium affects the location of the contact discontinuity with the CSM, which is determined by the balance between the thermal pressure of the shocked interstellar medium and the ram pressure of the wind (see e.g., Weaver et al. 1977; Matsuoka et al. 2022). When we consider cool and dense interstellar medium, the contact discontinuity should be located in the inner region due to the high thermal pressure of the shocked interstellar medium. If the interstellar medium is hot and more dilute, then the CSM would extend farther in the outer region.

- **Asphericity of the outflow:**

In this study, the outflows (stellar wind and the outflow from the Roche lobe) are assumed to be spherically symmetric, but non-spherical structures of the CSM can be realized. However, some studies suggested that if the outflow is via the Lagrangian point of the binary system, the CSM may be distributed along the equatorial plane with the spiral structure (Lubow & Shu 1975; Shu et al. 1979; Pejcha et al. 2016). Discussing the ejection mechanism and the resultant morphology of the outflow from the Roche lobe overflow would require multi-dimensional hydrodynamical models, which is beyond the scope of this paper. Nevertheless, we note that if the aspherical structure of the CSM is realized in SNe, they may leave unique signatures on radiative properties of SNe (e.g., Suzuki et al. 2019). We also mention that the circumstellar environment around red supergiants can be variable and even clumpy (e.g., VY Canis Majoris;

Smith et al. 2009). This implies that if the stellar wind from the primary has dense clumpy components, it can affect the multi-dimensional configuration of the CSM.

5. SUMMARY

In this paper, we have calculated mass-loss rates from a massive stars' binary system on the basis of non-conservative mass transfer during Roche lobe overflow. We demonstrate that the mass-transfer rate can vary with time according to the expansion or contraction of the stellar radius. If the Roche lobe overflow begins immediately after the exhaustion of the nuclear burning fuel in the core (e.g., hydrogen or helium), the mass-transfer rate can be intensively enhanced. In the framework of the non-conservative mass transfer in the binary, the time variability of the mass-transfer rate would be directly associated with the spatial inhomogeneity of the CSM density structure. By making use of hydrodynamics simulations we also showed that the abovementioned enhancement of the mass-transfer rate can emerge as the shell-like or cliff-like structures in the CSM. Particularly if the wind velocity is as slow as orders of 10 km s^{-1} , the characteristic radii in these CSM structures fall on $\sim 10^{17}$ cm and could contribute to the observational signatures traced by long-term observations of SNe.

Furthermore, we discussed the plausible processes that may yield the diversity of the CSM around SN progenitor, such as the choice of the primary mass. We found the stellar parameter set that can reproduce the significant increase in the mass-transfer rate, which could be comparable with the values implied for Type II SNe. Another parameter set is found that reproduces the mass-loss episode in the last 100 years before the explosion. This allows us to synthesize the inhomogeneous structure with the length and density scales compatible with the confined CSM proposed for infant Type II SNe, although fine tuning of the binary parameters would be required. We also mentioned other possible processes that can have influence on the configuration of the CSM. Our binary evolution models would highlight the possible scenario that explains the diversity of the CSM morphology inferred for SN progenitors.

Software: MESA revision 15140 (Paxton et al. 2011, 2013, 2015, 2018, 2019), PLUTO (Mignone et al. 2007, 2012). Inlists used to create the models are available on Zenodo under an open-source Creative Commons Attribution license: <https://doi.org/10.5281/zenodo.8385153>.

ACKNOWLEDGMENTS

The authors thank Ryoma Ouchi and Keiichi Maeda for providing the original calculation code, and Yudai

Suwa, Kenta Hotokezaka, and Daisuke Toyouchi, Ke-Jung Chen, and Nicolas Mauron for their helpful comments and suggestions. The authors are also grateful to the anonymous referee for his/her comments improving our manuscript. This work has been supported by the Japan Society for the Promotion of Science (JSPS) KAKENHI grants 20H01904 (TM), 21K13964, and 22KJ0528 (RS). This research is supported by the

National Science and Technology Council, Taiwan under grant No. MOST 110-2112-M-001-068-MY3 and the Academia Sinica, Taiwan under a career development award under grant No. AS-CDA-111-M04. Numerical simulations in this study were carried out in the supercomputer cluster Yukawa-21 equipped with Yukawa Institute for Theoretical Physics.

APPENDIX

A. LIFETIME OF THE STAR AT THE CARBON DEPLETION STAGE

To simplify the nucleosynthesis network calculations, we have approximated the carbon depletion time to the time when the primary star undergoes the core collapse (see Section 2.1). To check the validity of this assumption, we calculate the further evolution of a star with $M_{\text{ZAMS}} = 12 M_{\odot}$ after the carbon depletion in the core.

Figure A1 shows the result of the calculation up to the central carbon depletion stage adopted in this study (dashed black line) and up to the time of the core collapse (solid red line). The horizontal axis shows the logarithmic scale of the look-back time of the star measured from the core collapse. The ‘central carbon depletion stage’ is defined as when the central carbon abundance depletes below 10^{-6} , as described in the text, and ‘core-collapse’ is defined as when the infall-velocity in the central iron core exceeds 10^7 cm s^{-1} .

As can be seen in Figure A1, the result up to the central carbon depletion stage is stopped at a central temperature of $\log T_{\text{c}} = 9.1$ (i.e. $T \approx 1 \times 10^9 \text{ [K]}$), while the result up to the core collapse stage reaches the central temperature of $\log T_{\text{c}} = 9.8$ (i.e. $T_{\text{c}} > 5 \times 10^9 \text{ [K]}$). Figure A1 shows that the remaining time between the central carbon depletion phase and the core collapse is orders of ~ 10 years. Our discussion in the main text focused on the stellar properties with $t_{\text{lb}} \gg 10$ years, and this indicates that it is reasonable to approximate the central carbon depletion phase as the moment of the core collapse. We also note that both the lifetime of the star and the central temperature at the moment of the central carbon depletion stage are consistent with the properties suggested in Tur et al. (2010).

We have defined the mass fraction of carbon at the moment of entering the carbon depletion stage as 10^{-6} . It corresponds to the stage immediately before oxygen burning stage in the core. Since the timescale of the oxygen burning stage would not be largely affected by stellar properties such as stellar mass, we expect that our criterion of the carbon depletion stage is robustly tracing the epoch immediately before the core collapse, and the assumption of $t_{\text{end}} - t_{\text{cc}} = 10$ years is reasonable.

On the other hand, we find that there is a variation in the definition of the carbon depletion stage depending on the paper. Laplace et al. (2020) defines carbon depletion as the moment when the mass fraction of the carbon in the central core decreases below 10^{-4} . This results in the initiation of the carbon depletion 100 years before the core collapse. Ercolino et al. (2023) declares carbon depletion 10^3 years before the core collapse, and we expect this is due to the further higher criteria for the central carbon mass fraction.

B. COMPARISON BETWEEN THE ANALYTIC AND NUMERICAL SOLUTION OF THE CSM STRUCTURE

While we performed the numerical simulations of the CSM formation in Section 3.2, it is possible to rely on the analytical description of the wind structure. Piro & Lu (2020) presented the framework describing the hydrodynamical structure of the CSM originating from the time-dependent mass-loss history. Comparing these two methods allows us to confirm the application limit of the analytical treatment in the context of CSM formation.

Figure B1 shows the comparison between our numerical model and the analytical treatment with the binary parameter of $M_1 = 12 M_{\odot}$, $M_2 = 10.8 M_{\odot}$, $P_{\text{orb}} = 1300$ days. It is observed that these two treatments are compatible with each other within $r \sim 10^{18}$ cm. The corresponding look-back time of this radius is ~ 0.1 Myr, indicating that the time variation of the mass-loss rate after the helium exhaustion in the core can be directly associated with the density variation of the CSM. In this model, actually, the mass-loss rate is greatly enhanced immediately after the helium exhaustion, and this feature is clearly appearing as the shell-like structure around several times 10^{17} cm. We confirm the validity of the analytical treatment of time-dependent wind propagation in Piro & Lu (2020). In the outer region from $\sim 10^{18}$ cm, the thermal pressure of the interstellar medium heated by the wind’s shock prevents the

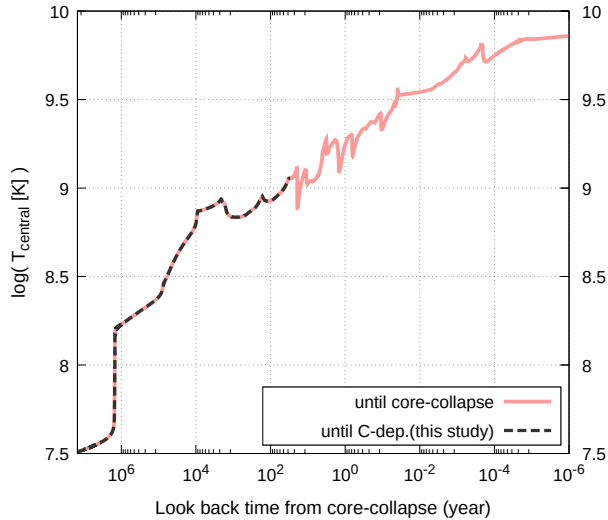


Figure A1. Time evolution of the central temperature of a single star with $M_{\text{ZAMS}} = 12 M_{\odot}$ as a function of look-back time from the core collapse. The red line shows the evolution until the core collapse of the Fe core, while the black dashed line indicates the same but until the carbon depletion, to highlight the treatment of our simulation.

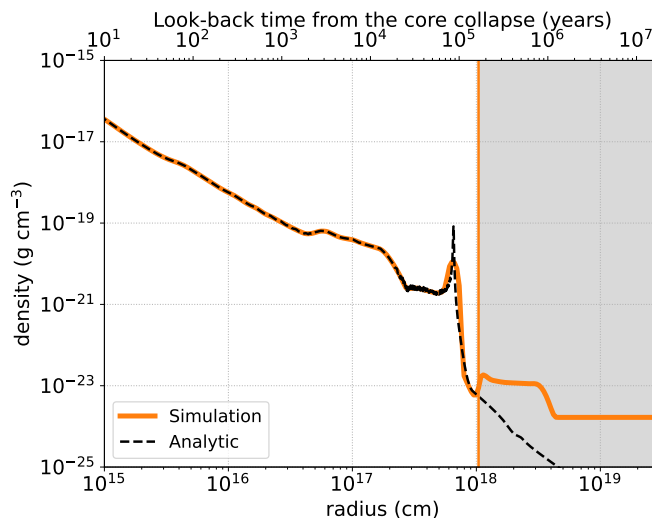


Figure B1. Comparison of the reconstructed CSM density structure between numerical (orange solid line) and analytic (black dashed line) solutions in the model with $M_1 = 12 M_{\odot}$, $M_2 = 10.8 M_{\odot}$, $P_{\text{orb}} = 1300$ days. The gray-shaded region on the right side indicates the deviation of the analytical solution from the numerical one.

further expansion of the stellar wind. Then the heated interstellar medium and the stellar wind would accumulate at the contact discontinuity, and the resultant CSM structure deviates from the analytical solution (see also Weaver et al. 1977; Matsuoka et al. 2022).

C. AN INTERPRETATION OF THE RADIAL EXPANSION OF THE PRIMARY STAR SUFFERING FROM MASS REMOVAL

A star suffering from the mass reduction expands its radius because of the increase in the gravitational energy compared to the internal energy, as explained in Section 3.1. In this section, we provide quantitative analysis on the response of the stellar radius to mass reduction on the basis of the polytrope sphere of gas.

Firstly let us consider a polytrope sphere of gas in hydrostatic equilibrium with the polytropic index n before the mass variation. As is known, we can solve the radial structure of the density of the polytrope sphere from equation of hydrostatic equilibrium and the Poisson equation (Kippenhahn & Weigert 1990). We can also write down the

gravitational energy of the system as

$$E_{\text{grav}} = -\frac{3}{5-n} \frac{GM^2}{R}, \quad (\text{C1})$$

where M and R are the mass and radius of the polytrope sphere, respectively. On the ground of the Virial theorem, the total energy of the gravitationally bounded system can be associated with the gravitational energy as follows: (Kippenhahn & Weigert 1990),

$$E_{\text{tot}} = \frac{3\gamma - 4}{3\gamma - 3} E_{\text{grav}} = -\left(\frac{3\gamma - 4}{3\gamma - 3}\right) \frac{3}{5-n} \frac{GM^2}{R} \equiv -F(\gamma, n) \frac{GM^2}{R}, \quad (\text{C2})$$

where γ is the specific heat ratio of the gas. For convenience, the coefficients relevant to γ and n are all absorbed in $F(\gamma, n)$, which we have newly introduced.

Next, we consider that a perturbation from an external force induces the stellar mass modification of δM , corresponding to the variation in the gravitational energy of the star δE and in the stellar radius of δR , but the system is still gravitationally bounded. For now we do not fix the sign of δM , δR , and δE . Then, by definition,

$$\delta E = -\int_R^\infty \frac{GM\delta M}{r^2} dr = -\frac{GM}{R} \delta M \quad (\text{C3})$$

is satisfied. The relationship among the perturbation terms is given as

$$\frac{\delta E}{E_{\text{tot}}} = 2 \frac{\delta M}{M} - \frac{\delta R}{R}. \quad (\text{C4})$$

Substituting the formulae of E_{tot} and δE into this equation, we can find out

$$\frac{\delta R}{R} = \left(2 - \frac{1}{F(\gamma, n)}\right) \frac{\delta M}{M}. \quad (\text{C5})$$

Note that when we consider mass reduction from the polytrope sphere, $\delta M/M$ is negative.

Equation (C5) clarifies the response of the stellar radius to the stellar mass variation. Figure C1 shows the radial expansion rate ($1 + \delta R/R$) as a function of the mass removal fraction $|\delta M/M|$ on the assumption of $\gamma = 5/3$. We plot the relationship with the polytrope index $n = 3/2$, which is plausible for the modeling for a star engulfed by a convective envelope (e.g., Matzner & McKee 1999). We also plot the numerical data obtained from our binary simulations in Section 3.1 to compare with the polytrope analysis. We can see that our binary models with $P_{\text{orb}} = 1300$ and 1500 days undergo the mass removal of 45 and 33% of the initial mass in total, and result in 15 and 11% of the radial expansion, respectively. These variations are in good agreement with the predictions from the analysis based on the polytrope sphere, which is illustrated by the black line. As for the model with $P_{\text{orb}} = 1100$ days, the expansion rate is suppressed to 14% while predicted as 18%. Anyway, our analysis based on the polytrope sphere can successfully explain $\sim 10\%$ of the radial expansions of the primary stars that suffer from the mass stripping in the binary. We expect that the precise quantification of the stellar radius should depend on the physics we have neglected, but that the inflation of ten percents of the stellar radius seen in our binary models can be robustly ascribed by the stripping of the envelope through binary interaction.

REFERENCES

- Angulo, C., Arnould, M., Rayet, M., et al. 1999, NuPhA, 656, 3, doi: [10.1016/S0375-9474\(99\)00030-5](https://doi.org/10.1016/S0375-9474(99)00030-5)
- Arnett, W. D., & Meakin, C. 2011, ApJ, 733, 78, doi: [10.1088/0004-637X/733/2/78](https://doi.org/10.1088/0004-637X/733/2/78)
- Asplund, M., Grevesse, N., Sauval, A. J., & Scott, P. 2009, ARA&A, 47, 481, doi: [10.1146/annurev.astro.46.060407.145222](https://doi.org/10.1146/annurev.astro.46.060407.145222)
- Balasubramanian, A., Corsi, A., Polisensky, E., Clarke, T. E., & Kassim, N. E. 2021, ApJ, 923, 32, doi: [10.3847/1538-4357/ac2154](https://doi.org/10.3847/1538-4357/ac2154)
- Beasar, E. R., Davies, B., Smith, N., et al. 2020, MNRAS, 492, 5994, doi: [10.1093/mnras/staa255](https://doi.org/10.1093/mnras/staa255)
- Bersten, M. C., Benvenuto, O. G., Nomoto, K., et al. 2012, ApJ, 757, 31, doi: [10.1088/0004-637X/757/1/31](https://doi.org/10.1088/0004-637X/757/1/31)

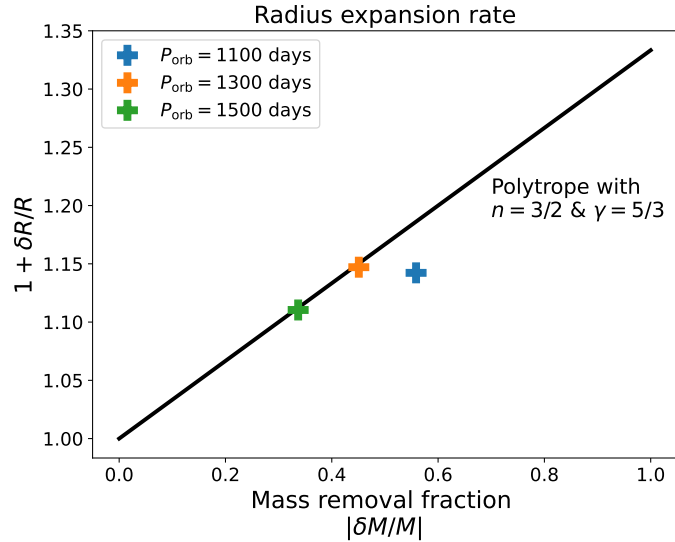


Figure C1. Radial expansion rates with response to the perturbation ($1 + \delta R/R$) as a function of the mass removal fraction $|\delta M/M|$ is illustrated on the assumption of $\gamma = 5/3$. Equation (C5) with $n = 3/2$ is plotted by the black solid line, while the numerical values obtained from our binary models in Section 3 are plotted by the thick cross points.

- Chandra, P., Chevalier, R. A., Chugai, N., Milisavljevic, D., & Fransson, C. 2020, *ApJ*, 902, 55, doi: [10.3847/1538-4357/abb460](https://doi.org/10.3847/1538-4357/abb460)
- Chevalier, R. A., & Fransson, C. 2017, in *Handbook of Supernovae*, ed. A. W. Alsabti & P. Murdin, 875, doi: [10.1007/978-3-319-21846-5_34](https://doi.org/10.1007/978-3-319-21846-5_34)
- Cyburt, R. H., Amthor, A. M., Ferguson, R., et al. 2010, *ApJS*, 189, 240, doi: [10.1088/0067-0049/189/1/240](https://doi.org/10.1088/0067-0049/189/1/240)
- de Jager, C., Nieuwenhuijzen, H., & van der Hucht, K. A. 1988, *A&AS*, 72, 259
- Draine, B. T. 2010, *Physics of the Interstellar and Intergalactic Medium* (Princeton University Press), doi: [doi:10.1515/9781400839087](https://doi.org/10.1515/9781400839087)
- Dwarkadas, V. V. 2005, *ApJ*, 630, 892, doi: [10.1086/432109](https://doi.org/10.1086/432109)
- . 2007, *ApJ*, 667, 226, doi: [10.1086/520670](https://doi.org/10.1086/520670)
- Eddington, A. S. 1926, *The Internal Constitution of the Stars*
- Eggleton, P. P. 1983, *ApJ*, 268, 368, doi: [10.1086/160960](https://doi.org/10.1086/160960)
- Ercolino, A., Jin, H., Langer, N., & Dessart, L. 2023, *arXiv e-prints*, arXiv:2308.01819, doi: [10.48550/arXiv.2308.01819](https://doi.org/10.48550/arXiv.2308.01819)
- Fang, Q., Maeda, K., Kunarayakti, H., Sun, F., & Gal-Yam, A. 2019, *Nature Astronomy*, 3, 434, doi: [10.1038/s41550-019-0710-6](https://doi.org/10.1038/s41550-019-0710-6)
- Farmer, R., Fields, C. E., Petermann, I., et al. 2016, *ApJS*, 227, 22, doi: [10.3847/1538-4365/227/2/22](https://doi.org/10.3847/1538-4365/227/2/22)
- Förster, F., Moriya, T. J., Maureira, J. C., et al. 2018, *Nature Astronomy*, 2, 808, doi: [10.1038/s41550-018-0563-4](https://doi.org/10.1038/s41550-018-0563-4)
- Fuller, J. 2017, *MNRAS*, 470, 1642, doi: [10.1093/mnras/stx1314](https://doi.org/10.1093/mnras/stx1314)
- Gilkis, A., Vink, J. S., Eldridge, J. J., & Tout, C. A. 2019, *MNRAS*, 486, 4451, doi: [10.1093/mnras/stz1134](https://doi.org/10.1093/mnras/stz1134)
- Heney, L., Vardya, M. S., & Bodenheimer, P. 1965, *ApJ*, 142, 841, doi: [10.1086/148357](https://doi.org/10.1086/148357)
- Herwig, F. 2000, *A&A*, 360, 952, doi: [10.48550/arXiv.astro-ph/0007139](https://doi.org/10.48550/arXiv.astro-ph/0007139)
- Hurley, J. R., Tout, C. A., & Pols, O. R. 2002, *MNRAS*, 329, 897, doi: [10.1046/j.1365-8711.2002.05038.x](https://doi.org/10.1046/j.1365-8711.2002.05038.x)
- Iglesias, C. A., & Rogers, F. J. 1996, *ApJ*, 464, 943, doi: [10.1086/177381](https://doi.org/10.1086/177381)
- Jacobson-Galán, W. V., Dessart, L., Jones, D. O., et al. 2022, *ApJ*, 924, 15, doi: [10.3847/1538-4357/ac3f3a](https://doi.org/10.3847/1538-4357/ac3f3a)
- Jacobson-Galan, W. V., Dessart, L., Margutti, R., et al. 2023, *arXiv e-prints*, arXiv:2306.04721, doi: [10.48550/arXiv.2306.04721](https://doi.org/10.48550/arXiv.2306.04721)
- Katsuda, S., Maeda, K., Bamba, A., et al. 2016, *ApJ*, 832, 194, doi: [10.3847/0004-637X/832/2/194](https://doi.org/10.3847/0004-637X/832/2/194)
- Kiewe, M., Gal-Yam, A., Arcavi, I., et al. 2012, *ApJ*, 744, 10, doi: [10.1088/0004-637X/744/1/10](https://doi.org/10.1088/0004-637X/744/1/10)
- Kilpatrick, C. D., Coulter, D. A., Foley, R. J., et al. 2022, *ApJ*, 936, 111, doi: [10.3847/1538-4357/ac8a4c](https://doi.org/10.3847/1538-4357/ac8a4c)
- Kilpatrick, C. D., Drout, M. R., Auchettl, K., et al. 2021, *MNRAS*, 504, 2073, doi: [10.1093/mnras/stab838](https://doi.org/10.1093/mnras/stab838)
- Kippenhahn, R., & Weigert, A. 1990, *Stellar Structure and Evolution*
- Ko, T., Tsuna, D., Takei, Y., & Shigeyama, T. 2022, *ApJ*, 930, 168, doi: [10.3847/1538-4357/ac67e1](https://doi.org/10.3847/1538-4357/ac67e1)
- Kolb, U., & Ritter, H. 1990, *A&A*, 236, 385

- Langer, N. 2012, *ARA&A*, 50, 107,
doi: [10.1146/annurev-astro-081811-125534](https://doi.org/10.1146/annurev-astro-081811-125534)
- Langer, N., El Eid, M. F., & Fricke, K. J. 1985, *A&A*, 145, 179
- Laplace, E., Götberg, Y., de Mink, S. E., Justham, S., & Farmer, R. 2020, *A&A*, 637, A6,
doi: [10.1051/0004-6361/201937300](https://doi.org/10.1051/0004-6361/201937300)
- Laplace, E., Justham, S., Renzo, M., et al. 2021, *A&A*, 656, A58, doi: [10.1051/0004-6361/202140506](https://doi.org/10.1051/0004-6361/202140506)
- Lubow, S. H., & Shu, F. H. 1975, *ApJ*, 198, 383,
doi: [10.1086/153614](https://doi.org/10.1086/153614)
- Lyman, J. D., Bersier, D., James, P. A., et al. 2016, *MNRAS*, 457, 328, doi: [10.1093/mnras/stv2983](https://doi.org/10.1093/mnras/stv2983)
- Maeda, K., Michiyama, T., Chandra, P., et al. 2023, *ApJL*, 945, L3, doi: [10.3847/2041-8213/acb25e](https://doi.org/10.3847/2041-8213/acb25e)
- Maeda, K., Chandra, P., Matsuoka, T., et al. 2021, *ApJ*, 918, 34, doi: [10.3847/1538-4357/ac0dbc](https://doi.org/10.3847/1538-4357/ac0dbc)
- Margutti, R., Kamble, A., Milisavljevic, D., et al. 2017, *ApJ*, 835, 140, doi: [10.3847/1538-4357/835/2/140](https://doi.org/10.3847/1538-4357/835/2/140)
- Martinez, L., Bersten, M. C., Anderson, J. P., et al. 2022, *A&A*, 660, A41, doi: [10.1051/0004-6361/202142076](https://doi.org/10.1051/0004-6361/202142076)
- Matsuoka, T., Lee, S.-H., Maeda, K., Takiwaki, T., & Moriya, T. J. 2022, *ApJ*, 930, 143,
doi: [10.3847/1538-4357/ac67a4](https://doi.org/10.3847/1538-4357/ac67a4)
- Matzner, C. D., & McKee, C. F. 1999, *ApJ*, 510, 379,
doi: [10.1086/306571](https://doi.org/10.1086/306571)
- Mauerhan, J. C., Filippenko, A. V., Zheng, W., et al. 2018, *MNRAS*, 478, 5050, doi: [10.1093/mnras/sty1307](https://doi.org/10.1093/mnras/sty1307)
- Maund, J. R., Smartt, S. J., Kudritzki, R. P., Podsiadlowski, P., & Gilmore, G. F. 2004, *Nature*, 427, 129, doi: [10.1038/nature02161](https://doi.org/10.1038/nature02161)
- Mauron, N. 1997, *A&A*, 326, 300
- Mauron, N., & Huggins, P. J. 1999, *A&A*, 349, 203
- Mauron, N., & Josselin, E. 2011, *A&A*, 526, A156,
doi: [10.1051/0004-6361/201013993](https://doi.org/10.1051/0004-6361/201013993)
- Mignone, A., Bodo, G., Massaglia, S., et al. 2007, *ApJS*, 170, 228, doi: [10.1086/513316](https://doi.org/10.1086/513316)
- Mignone, A., Zanni, C., Tzeferacos, P., et al. 2012, *ApJS*, 198, 7, doi: [10.1088/0067-0049/198/1/7](https://doi.org/10.1088/0067-0049/198/1/7)
- Moriya, T. J., Maeda, K., Taddia, F., et al. 2014, *MNRAS*, 439, 2917, doi: [10.1093/mnras/stu163](https://doi.org/10.1093/mnras/stu163)
- Moriya, T. J., Pruzhinskaya, M. V., Ergon, M., & Blinnikov, S. I. 2016, *MNRAS*, 455, 423,
doi: [10.1093/mnras/stv2336](https://doi.org/10.1093/mnras/stv2336)
- Moriya, T. J., Yoon, S.-C., Gräfener, G., & Blinnikov, S. I. 2017, *MNRAS*, 469, L108, doi: [10.1093/mnras/slx056](https://doi.org/10.1093/mnras/slx056)
- Morozova, V., Piro, A. L., Fuller, J., & Van Dyk, S. D. 2020, *ApJL*, 891, L32, doi: [10.3847/2041-8213/ab77c8](https://doi.org/10.3847/2041-8213/ab77c8)
- Morozova, V., Piro, A. L., & Valenti, S. 2017, *ApJ*, 838, 28,
doi: [10.3847/1538-4357/aa6251](https://doi.org/10.3847/1538-4357/aa6251)
- Nugis, T., & Lamers, H. J. G. L. M. 2000, *A&A*, 360, 227
- Ouchi, R., & Maeda, K. 2017, *ApJ*, 840, 90,
doi: [10.3847/1538-4357/aa6ea9](https://doi.org/10.3847/1538-4357/aa6ea9)
- Paxton, B., Bildsten, L., Dotter, A., et al. 2011, *ApJS*, 192, 3, doi: [10.1088/0067-0049/192/1/3](https://doi.org/10.1088/0067-0049/192/1/3)
- Paxton, B., Cantiello, M., Arras, P., et al. 2013, *ApJS*, 208, 4, doi: [10.1088/0067-0049/208/1/4](https://doi.org/10.1088/0067-0049/208/1/4)
- Paxton, B., Marchant, P., Schwab, J., et al. 2015, *ApJS*, 220, 15, doi: [10.1088/0067-0049/220/1/15](https://doi.org/10.1088/0067-0049/220/1/15)
- Paxton, B., Schwab, J., Bauer, E. B., et al. 2018, *ApJS*, 234, 34, doi: [10.3847/1538-4365/aaa5a8](https://doi.org/10.3847/1538-4365/aaa5a8)
- Paxton, B., Smolec, R., Schwab, J., et al. 2019, *ApJS*, 243, 10, doi: [10.3847/1538-4365/ab2241](https://doi.org/10.3847/1538-4365/ab2241)
- Pejcha, O., Metzger, B. D., & Tomida, K. 2016, *MNRAS*, 455, 4351, doi: [10.1093/mnras/stv2592](https://doi.org/10.1093/mnras/stv2592)
- Piro, A. L., & Lu, W. 2020, *ApJ*, 894, 2,
doi: [10.3847/1538-4357/ab83f6](https://doi.org/10.3847/1538-4357/ab83f6)
- Quataert, E., & Shiode, J. 2012, *MNRAS*, 423, L92,
doi: [10.1111/j.1745-3933.2012.01264.x](https://doi.org/10.1111/j.1745-3933.2012.01264.x)
- Sana, H., de Mink, S. E., de Koter, A., et al. 2012, *Science*, 337, 444, doi: [10.1126/science.1223344](https://doi.org/10.1126/science.1223344)
- Shiode, J. H., & Quataert, E. 2014, *ApJ*, 780, 96,
doi: [10.1088/0004-637X/780/1/96](https://doi.org/10.1088/0004-637X/780/1/96)
- Shu, F. H., Lubow, S. H., & Anderson, L. 1979, *ApJ*, 229, 223, doi: [10.1086/156948](https://doi.org/10.1086/156948)
- Smartt, S. J. 2009, *ARA&A*, 47, 63,
doi: [10.1146/annurev-astro-082708-101737](https://doi.org/10.1146/annurev-astro-082708-101737)
- Smith, N. 2017, in *Handbook of Supernovae*, ed. A. W. Alsabti & P. Murdin, 403,
doi: [10.1007/978-3-319-21846-5_38](https://doi.org/10.1007/978-3-319-21846-5_38)
- Smith, N., & Arnett, W. D. 2014, *ApJ*, 785, 82,
doi: [10.1088/0004-637X/785/2/82](https://doi.org/10.1088/0004-637X/785/2/82)
- Smith, N., Hinkle, K. H., & Ryde, N. 2009, *AJ*, 137, 3558,
doi: [10.1088/0004-6256/137/3/3558](https://doi.org/10.1088/0004-6256/137/3/3558)
- Soberman, G. E., Phinney, E. S., & van den Heuvel, E. P. J. 1997, *A&A*, 327, 620,
doi: [10.48550/arXiv.astro-ph/9703016](https://doi.org/10.48550/arXiv.astro-ph/9703016)
- Suzuki, A., Moriya, T. J., & Takiwaki, T. 2019, *ApJ*, 887, 249, doi: [10.3847/1538-4357/ab5a83](https://doi.org/10.3847/1538-4357/ab5a83)
- Tartaglia, L., Sollerman, J., Barbarino, C., et al. 2021, *A&A*, 650, A174, doi: [10.1051/0004-6361/202039068](https://doi.org/10.1051/0004-6361/202039068)
- Tauris, T. M., & van den Heuvel, E. P. J. 2006, in *Compact stellar X-ray sources*, Vol. 39, 623–665,
doi: [10.48550/arXiv.astro-ph/0303456](https://doi.org/10.48550/arXiv.astro-ph/0303456)
- Tenorio-Tagle, G., Bodenheimer, P., Franco, J., & Rozyczka, M. 1990, *MNRAS*, 244, 563
- Tenorio-Tagle, G., Rozyczka, M., Franco, J., & Bodenheimer, P. 1991, *MNRAS*, 251, 318,
doi: [10.1093/mnras/251.2.318](https://doi.org/10.1093/mnras/251.2.318)
- Timmes, F. X. 1999, *ApJS*, 124, 241, doi: [10.1086/313257](https://doi.org/10.1086/313257)

- Tinyanont, S., Lau, R. M., Kasliwal, M. M., et al. 2019, *ApJ*, 887, 75, doi: [10.3847/1538-4357/ab521b](https://doi.org/10.3847/1538-4357/ab521b)
- Tur, C., Heger, A., & Austin, S. M. 2010, *ApJ*, 718, 357, doi: [10.1088/0004-637X/718/1/357](https://doi.org/10.1088/0004-637X/718/1/357)
- Vink, J. S., de Koter, A., & Lamers, H. J. G. L. M. 2001, *A&A*, 369, 574, doi: [10.1051/0004-6361:20010127](https://doi.org/10.1051/0004-6361:20010127)
- Weaver, R., McCray, R., Castor, J., Shapiro, P., & Moore, R. 1977, *ApJ*, 218, 377, doi: [10.1086/155692](https://doi.org/10.1086/155692)
- Weil, K. E., Fesen, R. A., Patnaude, D. J., & Milisavljevic, D. 2020, *ApJ*, 900, 11, doi: [10.3847/1538-4357/aba4b1](https://doi.org/10.3847/1538-4357/aba4b1)
- Weiler, K. W., Williams, C. L., Panagia, N., et al. 2007, *ApJ*, 671, 1959, doi: [10.1086/523258](https://doi.org/10.1086/523258)
- Woosley, S. E., Heger, A., & Weaver, T. A. 2002, *Reviews of Modern Physics*, 74, 1015, doi: [10.1103/RevModPhys.74.1015](https://doi.org/10.1103/RevModPhys.74.1015)
- Wu, S., & Fuller, J. 2021, *ApJ*, 906, 3, doi: [10.3847/1538-4357/abc87c](https://doi.org/10.3847/1538-4357/abc87c)
- Wu, S. C., & Fuller, J. 2022, *ApJL*, 940, L27, doi: [10.3847/2041-8213/ac9b3d](https://doi.org/10.3847/2041-8213/ac9b3d)
- Yaron, O., Perley, D. A., Gal-Yam, A., et al. 2017, *Nature Physics*, 13, 510, doi: [10.1038/nphys4025](https://doi.org/10.1038/nphys4025)
- Yasuda, H., Lee, S.-H., & Maeda, K. 2021, *ApJL*, 919, L16, doi: [10.3847/2041-8213/ac24ac](https://doi.org/10.3847/2041-8213/ac24ac)
- . 2022, *ApJ*, 925, 193, doi: [10.3847/1538-4357/ac3b49](https://doi.org/10.3847/1538-4357/ac3b49)
- Yoon, S.-C. 2015, *PASA*, 32, e015, doi: [10.1017/pasa.2015.16](https://doi.org/10.1017/pasa.2015.16)
- Yoon, S.-C., Dessart, L., & Clocchiatti, A. 2017, *ApJ*, 840, 10, doi: [10.3847/1538-4357/aa6afe](https://doi.org/10.3847/1538-4357/aa6afe)
- Yoon, S. C., Woosley, S. E., & Langer, N. 2010, *ApJ*, 725, 940, doi: [10.1088/0004-637X/725/1/940](https://doi.org/10.1088/0004-637X/725/1/940)
- Zimmerman, E. A., Irani, I., Chen, P., et al. 2023, *arXiv e-prints*, arXiv:2310.10727. <https://arxiv.org/abs/2310.10727>